PERGAMON

Computers and Structures 79 (2001) 389–401

Computers & Structures

www.elsevier.com/locate/compstruc

Boundary element method for the strain-softening response of quasi-brittle materials in compression

Alberto Carpinteri *, Francesco Ciola [1], Nicola Pugno [1]

Department of Structural Engineering, Politecnico di Torino, Corso Duca degli Abruzzi 24, 10129 Torino, Italy

Received 6 August 1999; accepted 27 May 2000

Abstract

In the present paper, the mechanical compressive behavior of quasi-brittle materials is analyzed by means of an ad hoc boundary element algorithm. The analysis is carried out by taking into account the initial crack distribution, which cannot be neglected if the experimental reality (developing over three scales of observation, micro-, meso- and macro-scale) is to be modeled.

The algorithm permits us to follow the evolution of the crack geometry during the loading process, which is characterized, at each step, by the propagation of the most critical meso- or macro-crack. Moreover, in order to take into account the micro-crack effect causing the progressive decay of the material, a decreasing variation of the elastic modulus is assumed, depending on the strain energy density absorbed during the loading process.

Different geometries, with different slenderness and size scale, are analyzed by the proposed model, with and without friction between specimen and loading platens. The numerical simulations represent the experimental results consistently. © 2000 Elsevier Science Ltd. All rights reserved.

Keywords: Quasi-brittle; Compression; Strain-softening; Boundary element; Pseudo-traction; Multi-cracked finite plate; Experimental analysis; Numerical analysis

1. Introduction

The study of the compressive mechanical behavior of concrete, already analyzed by several authors, does not present till today a complete and systematic treatment, even if many salient aspects have been already emphasized. The most important of these aspects is constituted by the phenomenon of strain-softening that presents variable characteristics by varying the test conditions. There are in fact many parameters to be taken into account, of which two are the most important: the slenderness of the specimen and the friction between the specimen and the loading platens.

The present investigation highlights these aspects numerically and experimentally. An ad hoc algorithm based on the pseudo-traction [13–15] and on the boundary-element [5–7,10] methods was implemented and utilized for the numerical simulations. The experimental analysis was carried out at the ENEL-CRIS Laboratories in Milano [12] in the framework of the Round-Robin Test promoted by RILEM TC 148 SSC.

2. Pseudo-traction method

The application of the superposition principle permits to analyze the stress field in a linear elastic finite plate with one crack on the basis of well-known elementary schemes (Fig. 1). In Fig. 1(b) an infinite uncracked plate is depicted which is subjected to traction.

* Corresponding author. Tel.: +39-11-5644850; fax: +39-11-5644899.

E-mail addresses: carpinteri@polito.it (A. Carpinteri), pugno@polito.it (N. Pugno).

[1] Tel.: +39-11-5644902; fax: +39-11-5644899.

0045-7949/01/$ - see front matter © 2000 Elsevier Science Ltd. All rights reserved.
PII: S0045-7949(00)00149-8

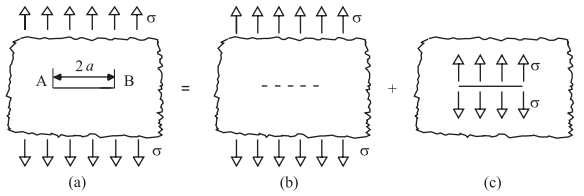

Fig. 1. (a) Infinite plate with one crack subjected to traction; (b) infinite uncracked plate subjected to traction; (c) infinite plate with one crack subjected to traction on its faces.

The scheme (a) of interest is equivalent to the sum of schemes (b) and (c) and the stress-intensity factor in A or B is the same as that in scheme (c) (fictitious stress field).

The pseudo-traction method (PTM) is based on the previous considerations. This method was developed by Horii and Nemat-Nasser [13], Kachanov and Montagut [14] and Kachanov [15] and it has been recently used by researchers interested in similar problems. For reference, see Ref. [9].

For scheme (c), it is possible to perform a stress field analysis. The solution was provided by Sneddon and Lowengrub [18]; they applied Westergaard's method and obtained the stress field in the cracked plate. In an analogous way, it is possible to solve the problem of a crack subjected to shearing stresses on its faces.

Via PTM, we can affirm that the known stress-intensity factors for scheme (c) are the same for scheme (a) of interest.

3. Infinite multicracked plate

The considerations presented in Section 2 can be extended to determine the stress-intensity factors in an infinite plate with several cracks. The superposition principle can be still applied considering in this case, three different schemes, as shown in Fig. 2.

In scheme (a), the plate is without crack and it is subjected to the stresses σ_{11}, σ_{12}, σ_{22} at the infinity; consequently, the stress field in the plate is practically assigned.

A more problematical situation appears in schemes (b) and (c). While in the scheme with only one crack it is immediate to determine the stress field in the plate, in a multicracked plate it is necessary to take into account the mutual interaction between the cracks.

In scheme (a), $\{\sigma_{1\infty}\}$ and $\{\sigma_{2\infty}\}$ are two vectors with the stress components σ_{xx}, σ_{xy}, σ_{yy} acting in points 1 and 2, respectively. In scheme (b), a stress field $-\{\sigma_{1\infty}\}$ in addition to the opposite of the stress field acting in 1 due to crack 2, acts on crack 1. The stress field acting in 1 is represented by the unknown vector $-\{\sigma_{12}\}$ with components $-\sigma_{xx}^{12}$, $-\sigma_{xy}^{12}$, $-\sigma_{yy}^{12}$. In an analogous way, if scheme (c) is taken into account, the stress field $-\{\sigma_{2\infty}\}$ in addition to the unknown vector $-\{\sigma_{21}\}$ due to the mutual interaction, acts on crack 2.

The problem is to determine the two vectors $\{\sigma_{12}\}$, $\{\sigma_{21}\}$. The normal and shearing stresses acting on crack 1 due to stress field $-\{\sigma_{1\infty}\}$ are indicated with $-\sigma_{1\infty}$ and $-\tau_{1\infty}$, respectively. The stresses $-\sigma_{2\infty}$ and $-\tau_{2\infty}$ have the same meaning for crack 2.

In scheme (b), the fictitious normal and shearing stresses as a whole acting on crack 1 (or on crack 2 in scheme (c) commuting the 1,2 indexes) are

$$\sigma_1 = -\Big(\sigma_{1\infty} + \sigma_{xx}^{12}\cos^2\alpha_1 + 2\sigma_{xy}^{12}\sin\alpha_1\cos\alpha_1 + \sigma_{yy}^{12}\sin^2\alpha_1\Big), \tag{1a}$$

$$\tau_1 = -\Big(\tau_{1\infty} + \Big(\sigma_{xx}^{12} - \sigma_{yy}^{12}\Big)\sin\alpha_1\cos\alpha_1 - \sigma_{xy}^{12}\big(\cos^2\alpha_1 - \sin^2\alpha_1\big)\Big) \quad (1 \leftrightarrow 2), \tag{1b}$$

where $\alpha_{1,2} = \vartheta_{1,2} + \pi/2$ is the crack orientation angle (Fig. 2).

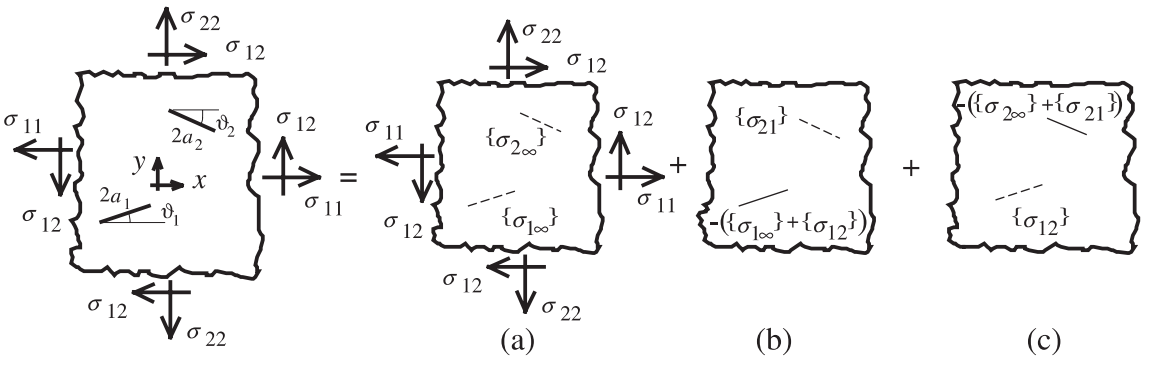

Fig. 2. Superposition principle to study an infinite multicracked plate.

Using the solution provided by Sneddon and Lowengrub [18] for the stress field in an infinite plate with one crack subjected to mixed mode, taking into account the crack orientation, it is possible to calculate for scheme (b) the stress field $\{\bar{\sigma}_{21}\}$ acting in point 2 and for scheme (c) the stress field $\{\bar{\sigma}_{12}\}$ acting in point 1. To verify the superposition principle expressed in Fig. 2, $\{\bar{\sigma}_{12}\}$ should be equal to $\{\sigma_{12}\}$ and $\{\bar{\sigma}_{21}\} = \{\sigma_{21}\}$; only in this case the cracks faces are free from stresses. Consequently, the following 12 relations can be written:

$$\bar{\sigma}_{ij}^{21} = \sigma_{ij}^{21} = \alpha_{ij}^{21}\sigma_1 + \beta_{ij}^{21}\tau_1, \quad ij = xx, xy, yy \qquad (1 \leftrightarrow 2), \tag{2}$$

where $\alpha_{ij}^{21}, \beta_{ij}^{21}$ $(1 \leftrightarrow 2)$ are known geometry-dependent coefficients [18].

Substituting 12 relations (2) into four equations (1), a linear system with four equations and four unknowns [20], representing the normal and shearing stresses acting on the crack surfaces, can be obtained:

$$\begin{aligned}\sigma_1 = -\Big(&\sigma_{1\infty} + \cos^2\alpha_1\left(\alpha_{xx}^{12}\sigma_2 + \beta_{xx}^{12}\tau_2\right)\\ &+ 2\sin\alpha_1\cos\alpha_1\left(\alpha_{xy}^{12}\sigma_2 + \beta_{xy}^{12}\tau_2\right)\\ &+ \sin^2\alpha_1\left(\alpha_{yy}^{12}\sigma_2 + \beta_{yy}^{12}\tau_2\right)\Big),\end{aligned} \tag{3a}$$

$$\begin{aligned}\tau_1 = -\Big(&\tau_{1\infty} + \sin\alpha_1\cos\alpha_1\Big[\left(\alpha_{xx}^{12}\sigma_2 + \beta_{xx}^{12}\tau_2\right)\\ &- \left(\alpha_{yy}^{12}\sigma_2 + \beta_{yy}^{12}\tau_2\right)\Big] - \left(\cos^2\alpha_1 - \sin^2\alpha_1\right)\\ &\times\left(\alpha_{xy}^{12}\sigma_2 + \beta_{xy}^{12}\tau_2\right)\Big) \quad (1 \leftrightarrow 2),\end{aligned} \tag{3b}$$

Indicating with $\{P\}$ the vector of components $-(\sigma_{1\infty}, \tau_{1\infty}, \sigma_{2\infty}, \tau_{2\infty})$ and with $\{S\}$ the vector of components $(\sigma_1, \tau_1, \sigma_2, \tau_2)$, the system can be written in the following form:

$$[R]\{S\} = \{P\}, \tag{4}$$

where $[R]$ is a (4×4) well-known matrix.

If the cracks are M, we can obtain a similar system where $[R]$ is a $(2M \times 2M)$ matrix. The solution gives the fictitious stresses acting on each crack and hence the stress-intensity factors can be calculated.

4. Boundary element method

In the case of a finite plate, we must consider the interactions among the cracks and between them and the boundary. The solution is obtained by the boundary element method (BEM) [5–7,10]. A plate is considered subjected on the boundary to a distribution of normal stresses σ_{n}^* and shearing stresses σ_{t}^* (Fig. 3a). In an infinite plate, a line coincident with the boundary of the finite plate is considered; the same line is divided into N elements and each element is subjected to normal and shearing stresses P_{n}^i and P_{t}^i (Fig. 3b). It is important to observe that they are not the same as those on the boundary of the finite plate but they cause on the boundary normal and shearing stresses coincident with them. The stresses produced on the boundary line by the stresses P_{n}^i and P_{t}^i can be written in the form

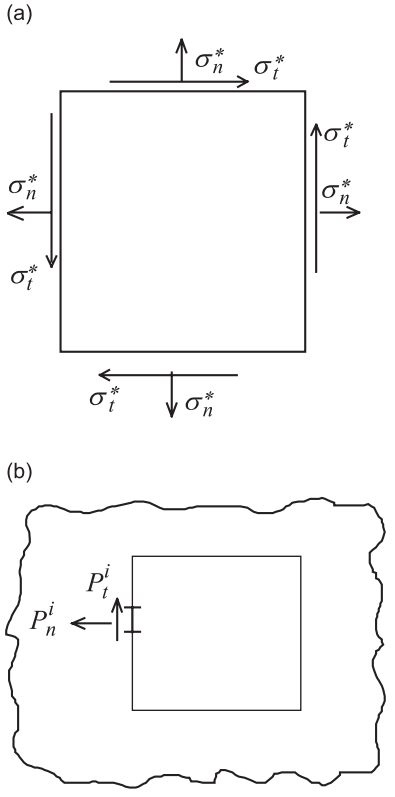

Fig. 3. (a) Finite plate and (b) infinite plate.

$$\sigma_{\mathrm{n}}^j = \sum_{i=1}^{N} A_{\mathrm{nn}}^{ij} P_{\mathrm{n}}^i + \sum_{i=1}^{N} A_{\mathrm{nt}}^{ij} P_{\mathrm{t}}^i, \tag{5a}$$

$$\sigma_{\mathrm{t}}^j = \sum_{i=1}^{N} A_{\mathrm{tn}}^{ij} P_{\mathrm{n}}^i + \sum_{i=1}^{N} A_{\mathrm{tt}}^{ij} P_{\mathrm{t}}^i, \tag{5b}$$

where $A_{\mathrm{nn,nt,tn,tt}}^{ij}$ are influence coefficients (well known by the BEM theory).

If we equalize for each element the stresses σ_{n}, σ_{t} to σ_{n}^*, σ_{t}^*, we can obtain a linear system with $2N$ equations and $2N$ unknowns. The solution gives the stresses P_{n}^i and P_{t}^i and then the stress field in the finite plate.

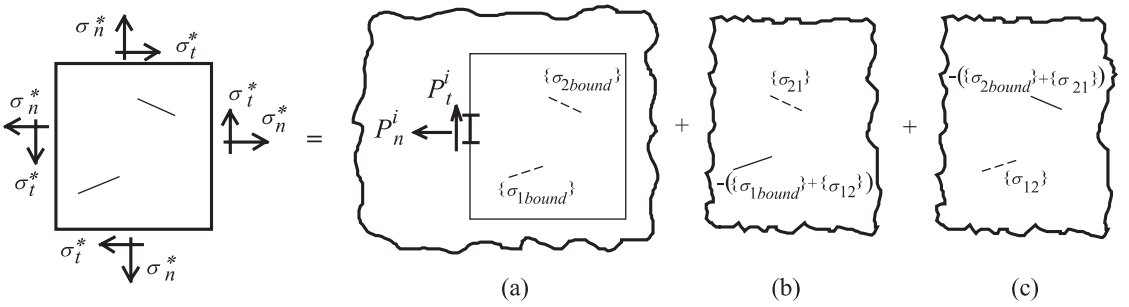

Fig. 4. Superposition principle to study a finite multicracked plate.

5. Pseudo-traction and boundary element methods

The formulations described in the last two sections can be combined together to determine the stress-intensity factors in a finite multicracked plate.

If a finite plate with two cracks is considered, the superposition principle can be applied to three different schemes (Fig. 4). Scheme (a) derives from the application of BEM. The stresses P_{n}^{i}, P_{t}^{i} create the two stress fields $\{\sigma_{1\mathrm{bound}}\}$ and $\{\sigma_{2\mathrm{bound}}\}$ acting in points 1 and 2, respectively. Schemes (b) and (c) present an infinite plate with crack 1 or 2, respectively. The procedure shown in Section 2 can be followed. Eqs. (1) and (3) substituting the subscript ∞ with *bound* are obtained, where $\{\sigma_{1\mathrm{bound}}\}$, $\{\sigma_{2\mathrm{bound}}\}$, differently from $\{\sigma_{1\infty}\}$, $\{\sigma_{2\infty}\}$, are unknown.

Due to the normal and shearing stresses P_{n}^{i}, P_{t}^{i} and to the stresses acting on the cracks, the following stresses act on the element j of the line-boundary, (scheme (a)):

$$\sigma_{\mathrm{n}}^{j}=\sum_{i=1}^{N}A_{\mathrm{nn}}^{ij}P_{\mathrm{n}}^{i}+\sum_{i=1}^{N}A_{\mathrm{nt}}^{ij}P_{\mathrm{t}}^{i}+B_{\mathrm{nn}}^{j1}\sigma_{1}+B_{\mathrm{nt}}^{j1}\tau_{1}+B_{\mathrm{nn}}^{j2}\sigma_{2}+B_{\mathrm{nt}}^{j2}\tau_{2}=\sigma_{\mathrm{n}}^{*},\tag{6a}$$

$$\sigma_{\mathrm{t}}^{j}=\sum_{i=1}^{N}A_{\mathrm{tn}}^{ij}P_{\mathrm{n}}^{i}+\sum_{i=1}^{N}A_{\mathrm{tt}}^{ij}P_{\mathrm{t}}^{i}+B_{\mathrm{tn}}^{j1}\sigma_{1}+B_{\mathrm{tt}}^{j1}\tau_{1}+B_{\mathrm{tn}}^{j2}\sigma_{2}+B_{\mathrm{tt}}^{j2}\tau_{2}=\sigma_{\mathrm{t}}^{*},\tag{6b}$$

where $A_{\mathrm{nn,nt,tn,tt}}^{ij}$ are coefficients coming from the BEM theory and $B_{\mathrm{nn,nt,tn,tt}}^{j1}$ $(1\leftrightarrow 2)$ are known from the Sneddon solution (Eq. (2)). As shown by the last equality, these must be equal to the stresses acting on the boundary of the finite plate and P_{n}^{i}, P_{t}^{i} become functions of the unknown fictitious stresses $\sigma_{1,2}$, $\tau_{1,2}$ acting on the crack faces.

From the BEM theory, it can be written as

$$\sigma_{1\mathrm{bound}}=\sum_{i=1}^{N}C_{\mathrm{nn}}^{1i}P_{\mathrm{n}}^{i}+\sum_{i=1}^{N}C_{\mathrm{nt}}^{1i}P_{\mathrm{t}}^{i},\tag{7a}$$

$$\tau_{1\mathrm{bound}}=\sum_{i=1}^{N}C_{\mathrm{tn}}^{1i}P_{\mathrm{n}}^{i}+\sum_{i=1}^{N}C_{\mathrm{tt}}^{1i}P_{\mathrm{t}}^{i}\quad(1\leftrightarrow 2),\tag{7b}$$

where $\mathrm{C}_{\mathrm{nn,nt,tn,tt}}^{1i}$ $(1\leftrightarrow 2)$ are known coefficients.

Substituting Eq. (7) into Eq. (3), where the subscript *bound* replaces the subscript ∞, and taking into account Eq. (6), a linear system of $(2N+4)$ equations and $(2N+4)$ unknowns can be obtained, the solution of which provided the $2N$ unknowns P_{n}^{i}, P_{t}^{i} and the four unknowns of fictitious stresses $\sigma_{1,2}$, $\tau_{1,2}$. From them we can obtain the stress-intensity factors at the tips of the cracks [18].

If the cracks are M, a similar system $2(M+N)\times 2(M+N)$ can be obtained. The solution gives the fictitious stresses acting on each crack and hence the stress-intensity factors can be calculated.

6. Determination of the structural compliance

In order to obtain the structural response, it is necessary to define a fundamental parameter represented by the global compliance. This is provided by two contributions: the former, C', is spread and depends on the

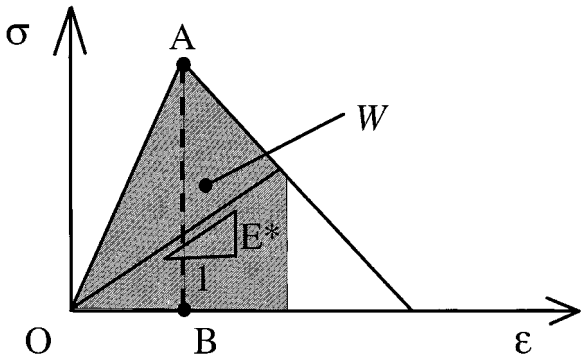

Fig. 5. Constitutive softening law of the material.

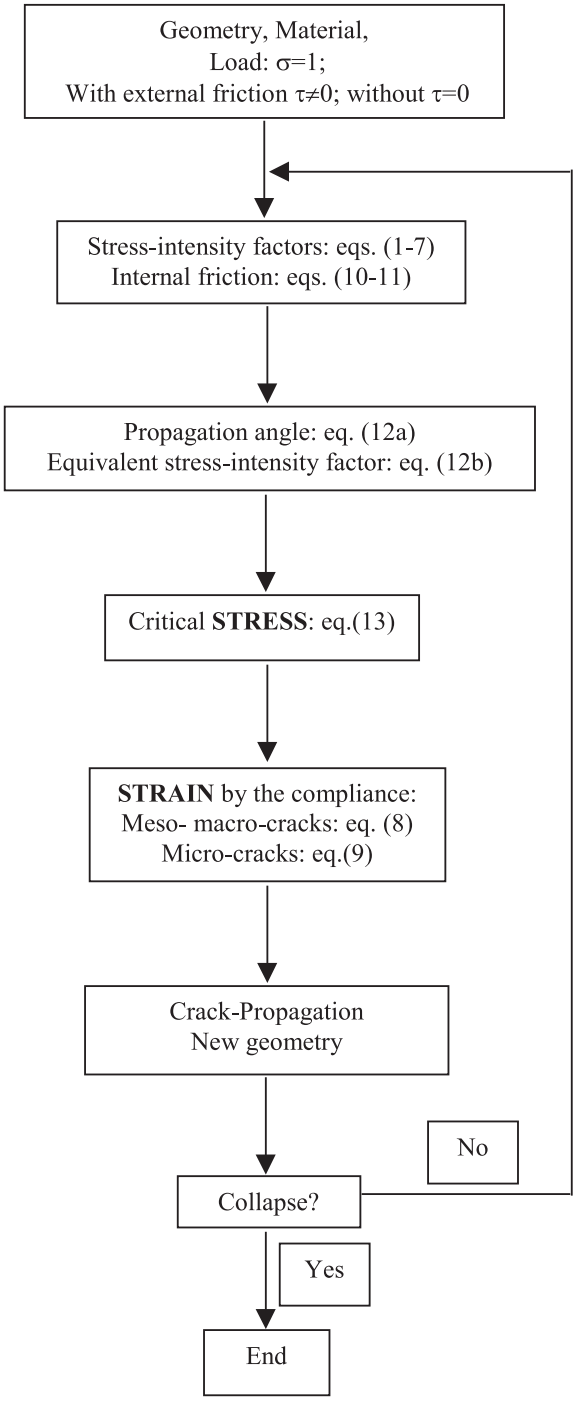

Fig. 6. Flow chart of the algorithm.

specimen dimensions and on the elastic modulus; the latter is due to the cracks and is called incremental compliance, C''. Both the compliances, C' and C'', vary during the loading simulation.

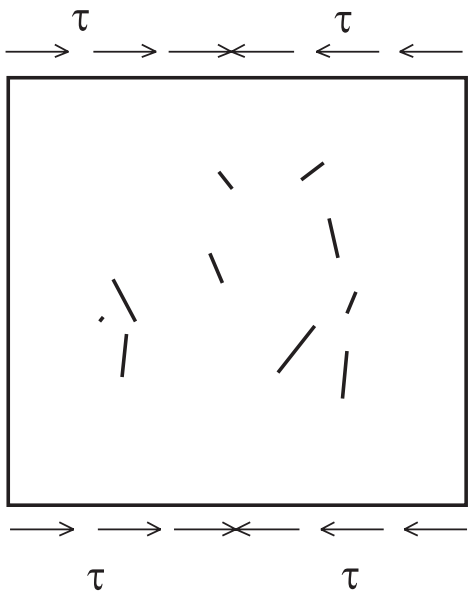

Fig. 7. Friction shearing stresses at the interfaces platens specimen.

If a crack is considered propagating, by virtue of Clapeyron's theorem and of the principle of conservation of energy, the following balance can be written:

$$\mathscr{G}_{\mathrm{I}} = \frac{1}{2}F^2\frac{\partial C}{\partial A} = \frac{K_{\mathrm{I}}^2}{E} + \frac{K_{\mathrm{II}}^2}{E}, \tag{8}$$

where $\mathscr{G}_{\mathrm{I}}$ is the fracture energy (per unit area), $K_{\mathrm{I,II}}$ the stress-intensity factor for Modes I and II, F the applied load, C the compliance of the cracked plate and A the crack surface. It is important to observe that $\partial C/\partial A$ is evidently equal to $\partial C''/\partial A$. From Eq. (8), the variation of C'' during the crack propagating can be calculated.

As regards the compliance contribution due to the material elasticity, the constancy assumption for the material elastic modulus does not reflect the physical evolution of the phenomenon. In fact, during the loading process, the microcracks, approximately distributed in a uniform manner, grow in the material, so that their macroscopic effect is the progressive decay of bulk elasticity. This particular aspect plays a fundamental role in the real behavior of the material.

In this work, as has already been stated in previous studies [4,8], the assumption we have put forward that the decay of the elastic modulus E^* (E is the initial elastic modulus) depends on the strain energy density W absorbed by the material during the loading process is (Fig. 5): the larger the energy absorbed, the lower the elastic modulus. This behavior can be described by the following function:

$$E^* = E\left(\frac{a}{W^{\alpha}} + b\right), \tag{9}$$

where E is the initial elastic modulus, $\alpha \cong 0.5$ (value approximately corresponding to a linear softening branch) and a, b are two constants respecting the two boundary conditions: the initial value (at the peak) of E^* is the real elastic modulus E and its limit final value (the extrapolated value where the stress vanishes) is zero. The initial value of W, its limit final value and the elastic modulus E are obtained as average values from the experimental curves.

7. Friction between the crack faces

When a compressive stress acts on the crack faces with friction, a shearing stress appears and tends to contrast the relative slip [3]:

$$\tau_{\text{fric}} = \lambda\sigma, \tag{10}$$

where λ is the friction (Coulomb) coefficient and σ, the normal stress. In this case, K_{I} is equal to zero being the crack closed.

If not only a normal but also a shearing stress τ acts on the crack its effect will be damped by the friction. If $|\tau| > |\lambda\sigma|$, the effective shearing stress will be

$$\tau_{\text{eff}} = \tau\left(1 - \frac{|\lambda\sigma|}{|\tau|}\right), \tag{11}$$

and K_{II} will be proportional to τ_{eff}.

If $|\tau| < |\lambda\sigma|$, τ_{eff} will be considered equal to zero, friction will prevent slippage, also K_{II} will be equal to zero.

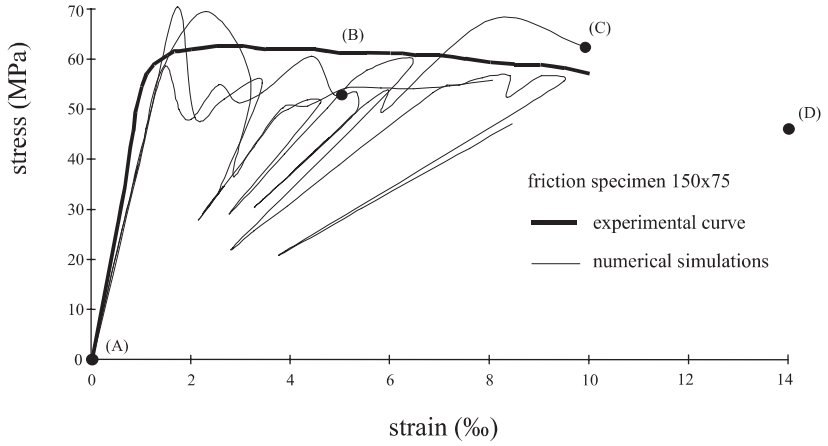

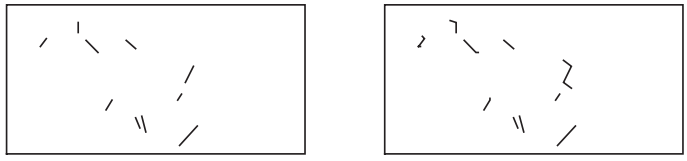

(A) initial crack distribution (B) intermediate crack distribution

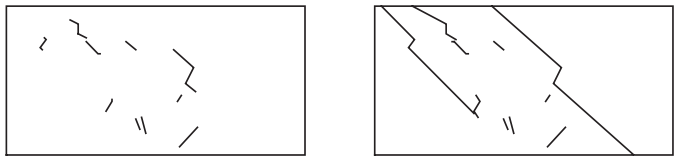

(C) crack distribution at the end of the diagram (D) collapse scheme

Fig. 8. Structural response and progressive cracked schemes (friction; specimen 150×75 mm^2).

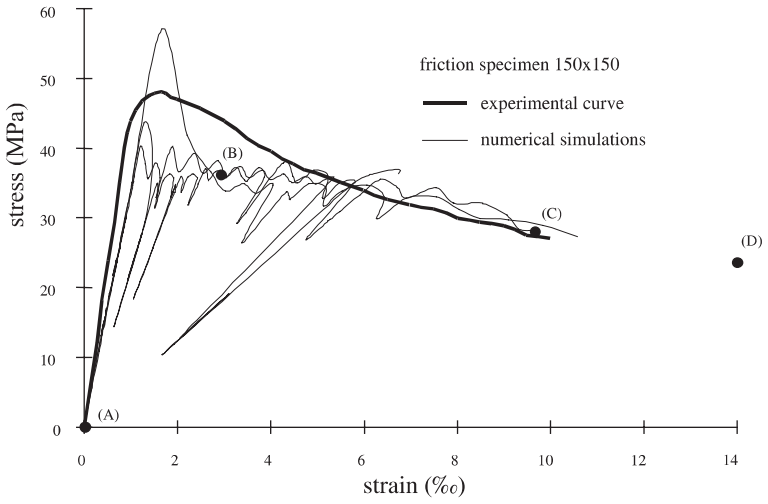

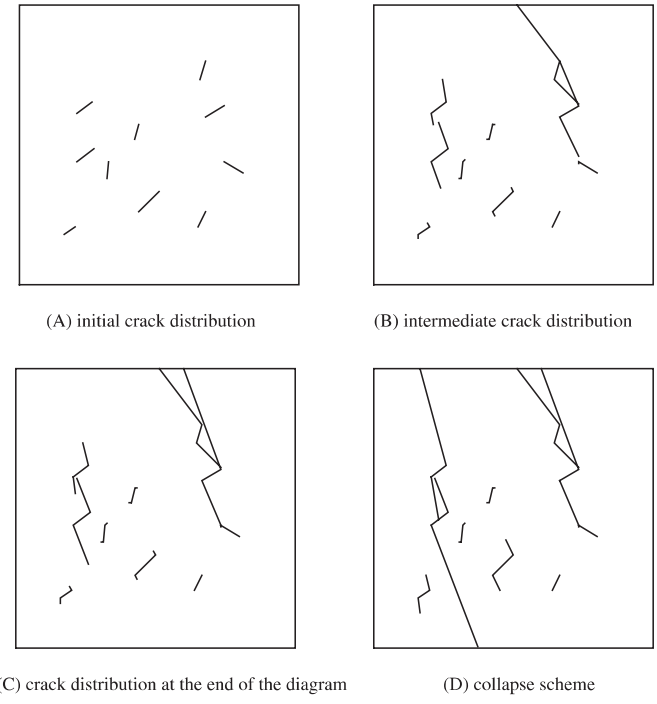

Fig. 9. Structural response and progressive cracked schemes (friction; specimen 150×150 mm^2).

8. Numerical modeling

In order to study the experiments in a realistic way, it is impossible to leave out of consideration the random distribution of cracks initially present in the material. In connection with what has been written above, a structural scheme constituted by a finite plate with a random distribution of initial meso- and macro-cracks is adopted in the numerical simulations. Considering this geometry and using the above mentioned formulation, the stress field and the stress-intensity factors acting on each crack are calculated (external load $\sigma = 1$).

Referring to the well-known maximum hoop stress criterion [11], for each crack tip a propagation angle θ and an equivalent stress-intensity factor K_{eq} can be calculated:

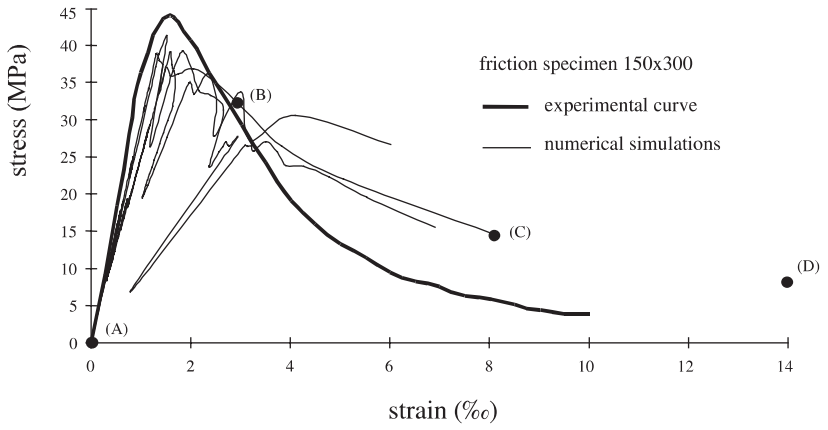

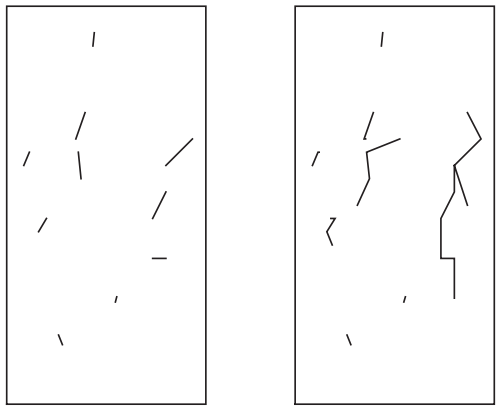

(A) initial crack distribution (B) intermediate crack distribution

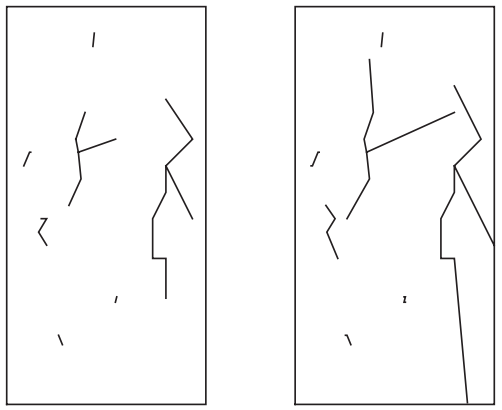

(C) crack distribution at the end of the diagram (D) collapse scheme

Fig. 10. Structural response and progressive cracked schemes (friction; specimen 150×300 mm^2).

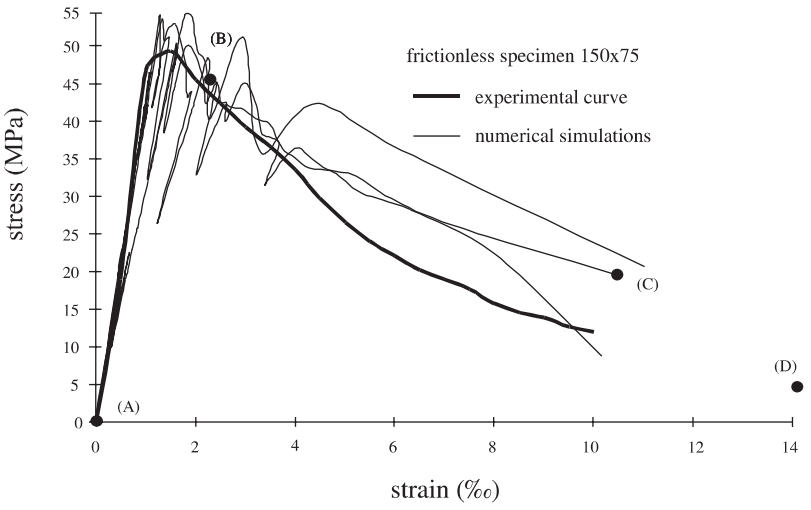

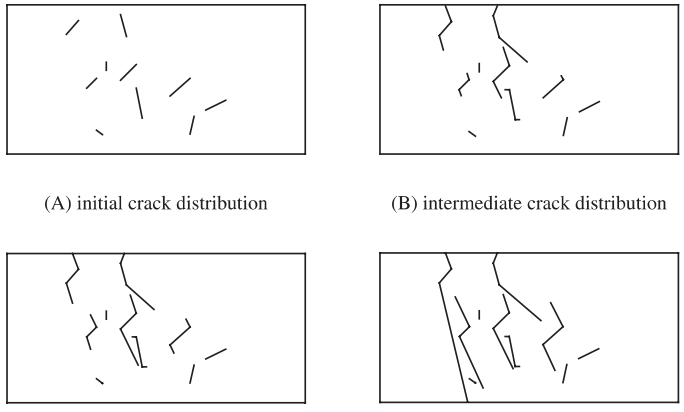

(A) initial crack distribution (B) intermediate crack distribution

(C) crack distribution at the end of the diagram (D) collapse scheme

Fig. 11. Structural response and progressive cracked schemes (frictionless; specimen 150×75 mm^2).

$$K_{\mathrm{I}} \sin\theta + K_{\mathrm{II}}(3\cos\theta - 1) = 0, \tag{12a}$$

$$K_{\mathrm{eq}} = \cos\frac{\theta}{2}\left[K_{\mathrm{I}}\cos^2\frac{\theta}{2} - \frac{3}{2}K_{\mathrm{II}}\sin\theta\right], \tag{12b}$$

where $K_{\mathrm{I,II}}$ are the stress-intensity factors calculated, as described, from the fictitious stresses acting on the cracks. Comparing the critical value K_{IC} with the highest K_{eq}, the external load of crack propagation can be calculated:

$$\sigma = K_{\mathrm{IC}}/K_{\mathrm{eq}}(\sigma = 1). \tag{13}$$

The next step is to cause the crack to propagate by a finite amount only at the tip where it is more solicited. At this stage, we are faced with a new geometry, on which it is necessary to carry out a fresh analysis. The procedure is then iterated until the specimen completely collapses (separation into at least two pieces). A flow chart of the algorithm is shown in Fig. 6.

9. Experimental results and numerical simulations

In this section, a comparison between the experimental results [12,17] and the numerical simulations will be presented. The experimental results regard prismatic specimens ($E = 336\,845$ kg/cm^2, $v = 0.15$, $\mathscr{G}_{\mathrm{I}} = 0.095$ kg/cm) with three different square bases (50×50, 100×100, 150×150 mm^2) and three different slendernesses (0.5, 1.0, 2.0), with and without friction between the specimen and the loading platens, for a total of 18 cases.

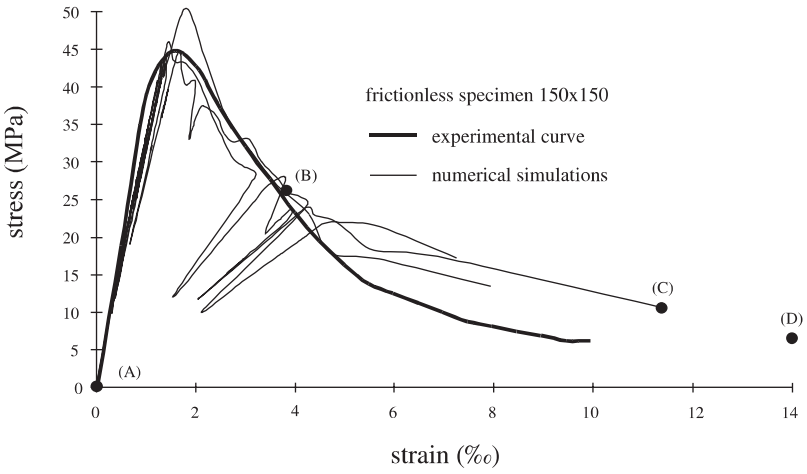

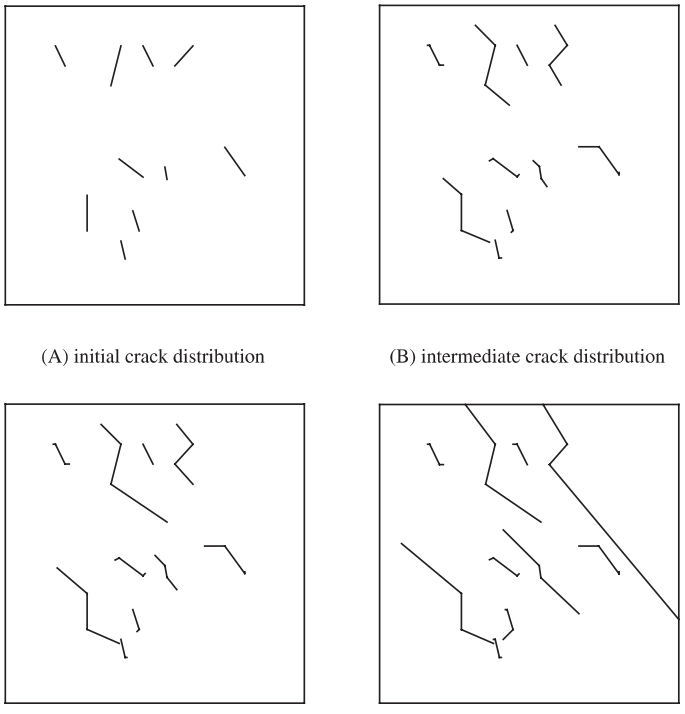

(A) initial crack distribution (B) intermediate crack distribution

(C) crack distribution at the end of the diagram (D) collapse scheme

Fig. 12. Structural response and progressive cracked schemes (frictionless; specimen 150×150 mm^2).

The friction condition is represented by the direct contact between specimen and platens, since the shearing stresses at the interface arise in opposition to the lateral expansion of the specimen. In the numerical simulations, this phenomenon is modeled by dividing the loaded boundaries in two parts and by imposing on each part a shearing stress τ directed inwards (Fig. 7). Each side of the specimen has been divided into 24 boundary elements.

On the other hand, the introduction of teflon layers between the specimen and the loading platens allows for the lateral expansion of the material; as a consequence,

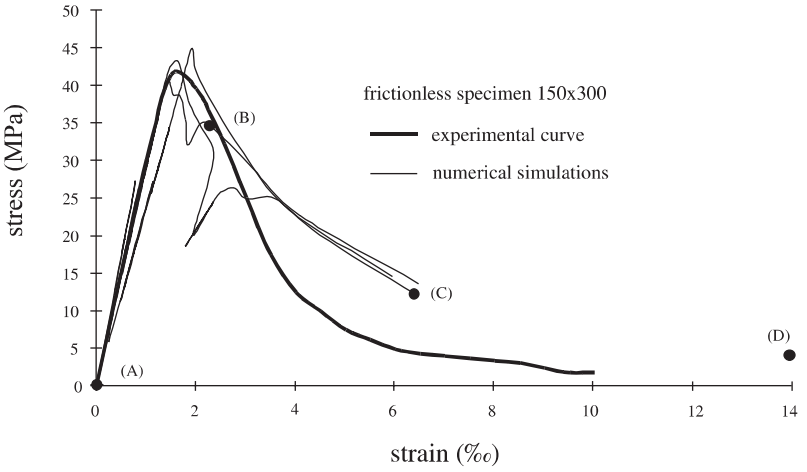

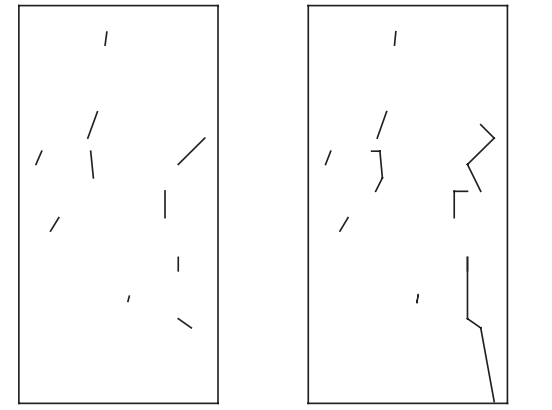

(A) initial crack distribution (B) intermediate crack distribution

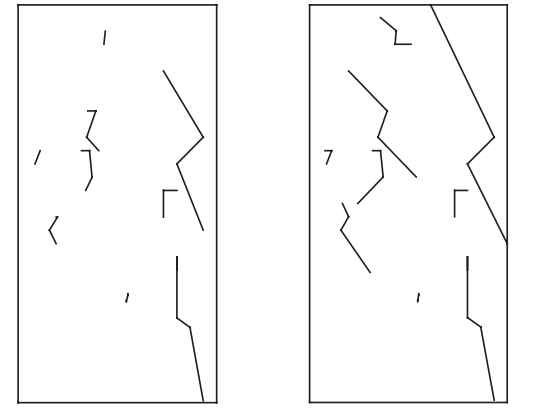

(C) crack distribution at the end of the diagram (D) collapse scheme

Fig. 13. Structural response and progressive cracked schemes (frictionless; specimen 150×300 mm^2).

the shearing stresses at the interface become negligible (the friction coefficient is close to 0.01). In the related numerical simulations at the boundary there is only the compressive normal stress.

For each experimental test, three numerical simulations with different initial crack patterns were carried out. Some numerical stress–strain curves and correspondent crack patterns are presented in Figs. 8–13. Snap-back instabilities are emphasized by the numerical simulations (crack-propagation controlled) not capturable by the experimental tests (displacement controlled). The numerical simulations emphasize the centrality of the cracking phenomenon in the structural response. Although the structural collapse is mainly governed by meso- and macro-cracks, at the same time it is very important to take into account the widespread elastic decay due to the presence of micro-cracks. It allows to capture the softening branch, which is typical of quasi-brittle materials and otherwise not reproducible [16].

If the stress–strain response is considered, some interesting aspects arise, which were also shown in other contributions [19]. First of all, it is important to highlight the friction influence: in the friction cases, there is a considerable variation in strength by varying the slenderness; the same trend is mitigated or even absent in frictionless cases. As a matter of fact, the frictional shearing stresses acting at the interface produce triaxially confined regions near the bases. For small slendernesses, the confined regions include most of the specimen (Fig. 14). As a consequence, the maximum loading capacity is higher for stubby specimens (it is well known that the triaxial compressive strength is usually larger than the uniaxial compressive strength). Hence, it is possible to explain the variation in strength by varying the slenderness in the friction tests, and the absence of this phenomenon when the teflon layers are used.

An additional important trend is represented by the ductility increase versus the specimen slenderness decrease. This trend, emerging more or less clearly in all the test results, is connected with and has a justification in the structural collapse schemes. When the slenderness decreases, a transition from *splitting* to *crushing* collapse occurs. The numerical simulations confirm the same trend. The *crushing* collapse, which is characterized by a multitude of micro-cracks, is associated with a larger energy dissipation during rupture and therefore with a more ductile behavior. On the other hand, the *splitting* collapse, which is characterized by a more localized rupture, requires a smaller energy dissipation and then produces a more brittle behavior. These aspects are also reflected in the numerical simulations [1,2]. In fact, the elastic modulus E^* (depending on the micro-cracks distribution) decays more rapidly when the specimen slenderness is lower (Fig. 15).

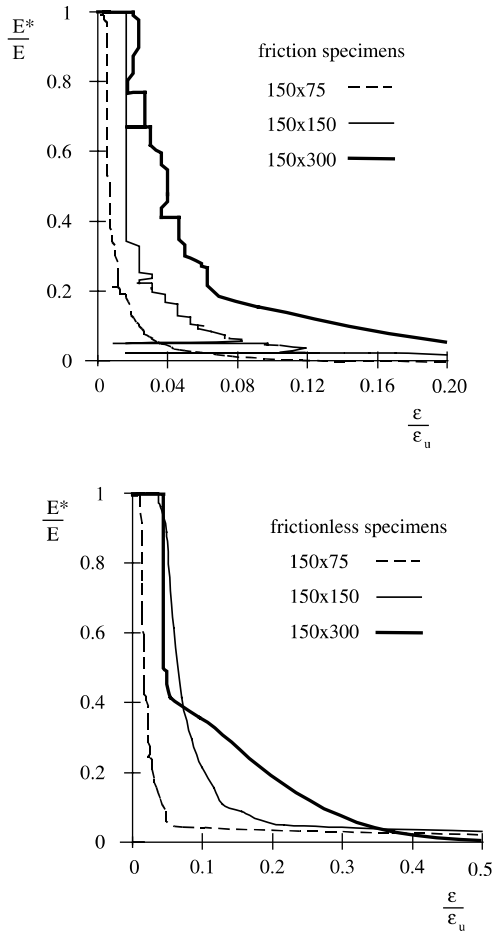

Fig. 15. Nondimensional diagram of elastic modulus versus strain, by varying the specimen slenderness (E is the initial elastic modulus and ε_u is the final strain).

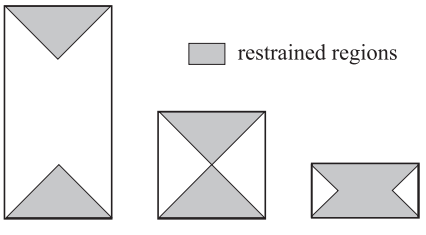

Fig. 14. Restrained regions in friction specimens.

10. Conclusions

The analysis of the results presented in the paper, based on the PTM and on the BEM, shows a satisfactory correspondence between the numerical simulations

and the experimental tests. The cases in which the unavoidable differences are more evident are those related to small and stubby specimens with friction. These differences are due to the fact that, in these conditions, the real specimen behavior moves away from the idealized plate behavior. The numerical model, however, gives good results in the other cases, and permits to predict the mechanical behavior of quasi-brittle materials.

Acknowledgements

The present research was carried out with the financial support of the Ministry of University and Scientific Research (MURST), the National Research Council (CNR) and the EC-TMR Contract No. ERB-FMRXCT960062. The original support from ENEL-CRIS is also acknowledged.

References

[1] Carpinteri A, Ciola F, Pugno N, Ferrara G, Gobbi ME. Applications of the boundary elements method to the compressive strain-softening behaviour of concrete. Proc FRAMCOS-III, 1998, Gifu, Japan. p. 1949–62.
[2] Carpinteri A, Ciola F, Pugno N. Numerical methods for the strain-softening response of concrete in uniaxial compression. Proc LOCALISED DAMAGE, 1998, Bologna, Italy. p. 297–306.
[3] Carpinteri A, Di Tommaso A, Viola E. Stato limite di frattura nei materiali fragili. Giornale del Genio Civile 1978;4–6:201–24.
[4] Carpinteri A, Sih GC. Damage accumulation and crack growth in bilinear materials with softening: application of strain energy density theory. Theoret Appl Fract Mech 1984;1:145–60.
[5] Carpinteri A, Yang GP. Fractal dimension evolution of microcrack net in disordered materials. Theoret Appl Fract Mech 1996;25:73–81.
[6] Carpinteri A, Yang GP. Damage process in finite sized brittle specimen with interacting microcracks. Fract Fatigue Engng Mater Struct 1997;20:1105–15.
[7] Carpinteri A, Yang GP. Size effects in brittle specimen with microcrack interaction. Comput Struct 1997;63:429–37.
[8] Carpinteri A. Mechanical damage and crack growth in concrete. Dordrecht: Martinuus Nijhoff; 1986.
[9] Ciola F. Effetti di Scala sul Comportamento Meccanico a Compressione del Calcestruzzo. PhD Thesis, Politecnico di Torino, Italy, 1998.
[10] Crouch SL, Starfield AM. Boundary element methods in solid mechanics. London: George Allen and Unwin; 1983.
[11] Erdogan F, Sih GC. On the crack extension in plates under plane loading and transverse shear. J Basic Engng 1963; 85:519–27.
[12] Ferrara G, Gobbi ME. Strain softening of concrete under compression. Report to RILEM Committee 148 SSC, ENEL-CRIS Laboratory, Milano, Italy, 1995.
[13] Horii H, Nemat-Nasser S. Elastic field of interacting inhomogeneities. Int J Solids Struct 1985;21:731–45.
[14] Kachanov M, Montagut E. Interaction of crack with certain microcrack arrays. Engng Fract Mech 1986;25:625–36.
[15] Kachanov M. Elastic solids with many cracks and related problems. Adv Appl Mech 1987;30:259–445.
[16] Monetto I. Evoluzione della frattura nelle lastre multifessurate. PhD Thesis, Politecnico di Torino, Italy, 1997.
[17] RILEM Round Robin Test. Strain Softening of Concrete in Uniaxial Compression. Report of the Round Robin Test carried out by RILEM TC 148 SSC, Mater Struct 1997;30:195–209.
[18] Sneddon NI, Lowengrub M. Crack problems in the classical theory of elasticity. New York: Wiley; 1969.
[19] Van Mier JGM. Strain softening of concrete under multiaxial compression. PhD Thesis, Eindhoven University of Technology, Netherlands, 1984.
[20] Yang GP, Liu XL. Microcracks interaction in concrete. Int Symp Concrete Engng, Nanjing, 1991.